Perturbation of charge density waves in $1T$-TiSe$_2$

Imrankhan Mulani ©, Umashankar Rajput ©, Luminita Harnagea ©, and Aparna Deshpande ©

Indian Institute of Science Education and Research (IISER) Pune, Dr. Homi Bhabha Road, Pashan, Pune 411008, India

In this paper, using low-temperature scanning tunneling microscopy, we focus on understanding the native defects in pristine $1T$-TiSe$_2$ at the atomic scale. We probe how they perturb charge density waves (CDWs) and lead to local CDW modulated region formation. These defects influence the correlation length of CDWs. We establish a connection between suppression of CDWs and Ti intercalation, and show how this supports the exciton condensation model of CDW formation in $1T$-TiSe$_2$.

I. INTRODUCTION

Transition metal dichalcogenides (TMDCs) are versatile materials that exhibit phenomena like strongly correlated phases to multifaceted tunable properties for applications in flexible electronics, optoelectronics, spintronics, and energy harvesting [1–4]. Many exotic physical phenomena, like spin-valley interaction, exciton-polariton states, and charge density wave (CDW) states are observed in TMDCs. TMDCs have a characteristic layered structure, tunable band gap, and strong spin-orbit coupling favoring such applications. The chemical composition of TMDCs is of the form MX_2 where M denotes transition metals (like Ti, Mo, and W) and X represents chalcogens (like S, Se, and Te). Despite having a similar structure, these materials can be categorized as insulating, semiconducting, semimetallic, metallic, or superconducting, depending on their chemical composition. The nonbonding d band and the extent of its electron filling endow these compounds with diverse properties. Bulk crystals of TMDCs consist of two-dimensional (2D) layers bonded by weak van der Waals interactions, rendering them easy to exfoliate. Depending on the arrangements of the atoms, structural polytypes of 2D TMDCs can be categorized as $1T$ (tetragonal symmetry with octahedral coordination), $2H$ (hexagonal symmetry with trigonal prismatic coordination), and $3R$ (rhombohedral symmetry with trigonal prismatic coordination). The layer degree of freedom provides an additional parameter to tune the properties of TMDCs [5].

One of the group-IV TMDCs hosting interesting properties is $1T$-TiSe$_2$. It is a semimetal with a small indirect band gap [6]. At temperature $T_{CDW} \sim 200$ K, $1T$-TiSe$_2$ undergoes a second-order phase transition to the CDW phase [7]. A CDW is a many-body, correlated electron phenomenon, where a periodic distortion modulates electron density. CDWs, depending on the ratio of their wavelength and lattice parameters, are classified as commensurate (CCDW), nearly commensurate (NCCDW), or incommensurate (ICDW) [8,9]. Pristine $1T$-TiSe$_2$ shows CCDW order below 200 K [7]. Charge carrier doping via electrochemical ionic gating in $1T$-TiSe$_2$ leads to suppression of CCDWs and the emergence of ICDWs and superconducting phases at lower temperature [10]. The CDW transition temperature drops significantly for $1T$-TiSe$_2$ doped with copper. Superconductivity emerges in Cu$_x$TiSe$_2$ for $x \sim 0.04$, the maxima of the superconducting transition temperature reaches at $x \sim 0.08$ [11]. The ICDW phase coexists with the superconducting phase under applied pressure [12] and copper doping [13]. The mechanism of formation of CDWs in $1T$-TiSe$_2$ is still a matter of debate. The two favored mechanisms are the excitonic insulator phase [14] and the band-type Jahn-Teller effect [15]. Excitons are bound states of electrons and holes. Excitons are bosons and can form a Bose-Einstein condensate [16–19]. The excitonic insulator phase can arise in a small gap semiconductor or semimetal, where excitons form spontaneously because of low carrier density to screen the attractive Coulomb interaction between electrons and holes. In the Jahn-Teller effect, the lattice spontaneously distorts to lift the degeneracy and reach the lower symmetry state because of the interaction between phonons and degenerate electron states. The Jahn-Teller-like mechanism is independent of free carrier concentration.

$1T$-TiSe$_2$ is a nonstoichiometric compound. The concentration of Ti in a crystal depends on the temperature at which the crystal is grown. A commonly used method for TMDC crystal growth is chemical vapor transport (CVT). Higher growth temperatures generate higher chalcogen pressures, resulting in a crystal with intercalation of metal [20]. An indirect inference of the presence of excess Ti can be carried out through temperature-dependent resistivity measurements. $1T$-TiSe$_2$ shows an anomalous resistivity peak near the CDW phase transition. As the growth temperature increases, the crystal becomes more metallic due to excess Ti and hence suppresses the anomalous resistivity peak [7,21]. $1T$-TiSe$_2$ shows a small indirect band gap above the transition temperature $T_{CDW} \sim 200$ K [22,23]. Angle-resolved photo emission spectroscopy experiments show a small band gap below the CDW transition [24]. Recent experimental evidence suggests an excitonic insulator mechanism [25–30]. Theoretical investigations suggest that excitonic condensation can be either superfluid [31] or an insulator [32]. A chiral nature of CDWs in pristine and Cu-doped $1T$-TiSe$_2$ has been reported using

polarized optical reflectometry and scanning tunneling microscopy (STM) [33–35]. Suppression of CDWs results in a superconducting phase transition with application of pressure [36] via electrostatic gating [10] or with Cu intercalation [11] or Pd intercalation [37]. $1T$-TiSe$_2$ becomes insulating after Pt doping [38]. This implies that doping affects the nature of CDWs and electronic properties of $1T$-TiSe$_2$.

A correlated phenomenon, like CDWs, is sensitive to the presence of defects. Here, using low-temperature STM, we focus on the behavior of CDWs at the atomic scale in the presence of intrinsic defects. We investigated the relationship between growth conditions and intrinsic defects in crystals grown by different synthesis routes. We referred to them as sample A [crystal was grown by CVT using iodine (I$_2$)] and sample B (crystal was grown using Se as self-flux) in the subsequent discussion.

II. METHODS

The experiments were performed by using an Omicron ultrahigh vacuum (UHV) low-temperature scanning tunneling microscope (STM) at 77 K with a base pressure of 5×10^{-11} mbar. Two $1T$-TiSe$_2$ crystals were studied. Sample A was grown using CVT with I_2 as the transport agent. Sample B was synthesized using the flux zone method by 2D Semiconductors, USA [39]. For STM studies of both samples, a $1T$-TiSe$_2$ single crystal surface was prepared by cleaving it in the UHV sample preparation chamber. The surface quality was checked with STM at 77 K. A clean surface at the atomic level was inferred from several STM images of different scan sizes. Electrochemically etched tungsten (W) tips were used for imaging. Several trials of imaging were performed with different tips. Topography measurements were taken in constant current mode. In our setup, bias voltage is applied to the sample. The images were processed using the image analysis software SPIP 6.0.9 (Image Metrology). MATLAB (by The MathWorks Inc.) was used for numerical calculations.

III. RESULTS AND DISCUSSION

$1T$-TiSe$_2$ crystal is a stack of monolayers bonded by van der Waals interaction. Each monolayer consists of titanium (Ti) atoms sandwiched between two sheets of selenium (Se) atoms [Fig. 1(a)]. Each Ti atom is surrounded by six Se atoms in octahedral coordination, as shown in Fig. 1(a). The space group of $1T$-TiSe$_2$ is $P\bar{3}m1$ (No. 164). The crystal cleaves along (001) planes exposed Se atoms in a hexagonal symmetric pattern. In constant current topography images, a STM tip probes the topmost Se atoms [40,41]. The tunneling current is mainly due to the contribution from the $4p$ orbital of Se atoms. The preferred site for Ti atom intercalation is schematically shown in Fig. 1(b), whereas the O substitution site is shown in Fig. 1(c). Iodine is used as a transport agent in a CVT method of crystal growth. Substitution of Se atoms by I is another defect commonly found in CVT-grown samples. I substitution occupies the same sites as O substitution. Defects in the STM topography image of sample A in Fig. 1(d) and sample B in Fig. 1(e) show up as localized bright regions. Note that the defects are less in sample B than in sample A.

In Fig. 1(d), the inset, yellow rounded rectangle, shows the enlarged atomic-scale image of the defect, which can be
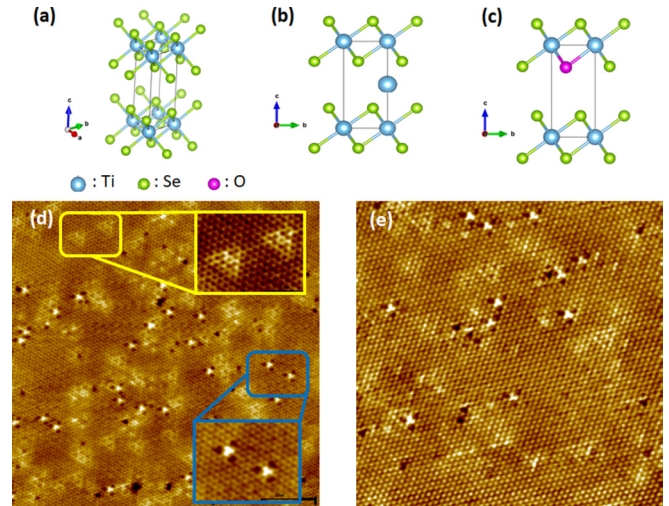

FIG. 1. (a) Schematics of $1T$-TiSe$_2$ unit cell viewed from an angle, Ti atoms in octahedral coordination, Se atoms form a triangular lattice. (b) Schematics of Ti intercalation site 2g. (c) Schematic of O substitution site. (d) Empty-states constant current STM image of 30 nm × 30 nm area of sample A. Enlarged view of Ti intercalation sites are in yellow rounded rectangle inset and that of O substitution sites are in blue rounded rectangle inset. $V_{bias} = 300$ mV and $I_{set} = 300$ pA. (e) Empty-states constant current STM image of 20 nm × 20 nm area of sample B, $V_{bias} = 300$ mV and $I_{set} = 500$ pA.

identified as a Ti intercalation site. Intercalated atoms occupy octahedral sites or tetrahedral sites in the van der Waals gap. For Ti, favorable sites are octahedral sites because of their more significant coordination number, and spacing between two nearby octahedral sites is more considerable than tetrahedral sites [42]. The characteristic appearance of intercalated Ti sites can be attributed to a change in the local density of states (DOS) [43]. These defects appear bright in filled-states STM images (at negative bias voltages).

There were defects with a strongly localized DOS at the topmost Se atoms surrounded by a depleted region in empty-state STM images (at positive bias voltages). Those defects can be identified with oxygen (O) substitution of the Se atom in the lower layer. I substitution sites are hard to recognize as they appear very faint compared to O sites [41]. Substitution of Se by O or I on the topmost layer is not favored energetically [41]. Oxygen, present as an impurity in iodine and a selenium precursor during growth, acts as a native dopant. Sample A has been observed to possess more Ti intercalation sites than sample B [Figs. 1(d) and 1(e)]. Using STM images taken in different regions of both samples, the average number of intercalation sites were counted. Employing this method, we found that the average count of Ti intercalation sites per unit cell for sample A is 0.6% as compared to 0.2% sites per unit cell for sample B. This observation supports the dependence of Ti intercalation sites' concentration on sample growth conditions [7].

Intercalation and substitution change the material's carrier concentration, leading to a change in the material's electronic properties. Correlated states like CDWs are sensitive to external factors like mechanical stress, external pressure, and carrier concentration. Point defects can affect CDWs by
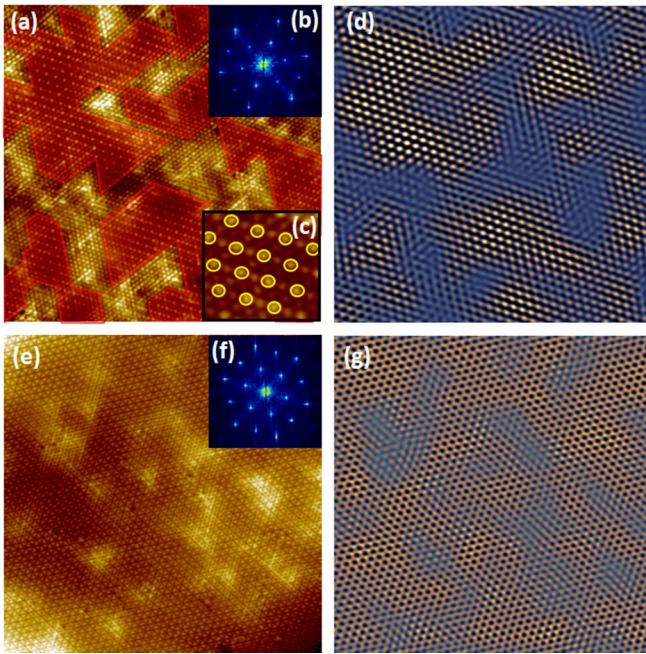
FIG. 2. (a) Filled-states constant current STM image of 30 nm $\times$ 30 nm area of sample A grown by CVT method, $V_{bias} = -400$ mV $I_{set} = 300$ pA. Areas marked by red are CDW-modulated regions, separated by nonmodulated regions induced by Ti intercalation sites. (b) Fourier transform of topography image in (a). (c) An enlarged image showing 2×2 superstructure with CDW peaks marked by yellow circles (d) Selective inverse Fourier transform of CDW peaks in (b), (e). Filled-states constant current STM image of 30 nm $\times$ 30 nm area of sample B grown by flux zone method, $V_{bias} = -300$ mV $I_{set} = 400$ pA. (f) Fourier transform of topography image in (e). (g) Selective inverse Fourier transform of CDW peaks in (f).

changing carrier density locally and introducing localized distortions in lattice [20]. STM topography images were obtained at different bias voltages, spatially resolving the CDWs. Figures 2(a) and 2(e) show STM images of samples A and B with different Ti intercalation and O substitution densities. Real-space topography shows the clear 2×2 superlattice of the CDW. Figure 2(c) is an enlarged image with atomic resolution showing CDWs forming superstructures (marked by yellow circles). Fourier transform (FT) of topography images [Figs. 2(b) and 2(f)] yields contributions of the lattice and CDW superlattice as sixfold symmetry peaks. Peaks in FT images affirm that the wavelength of CDW is twice the lattice spacing (first-order Bragg peak). To reduce background noise and understand the spatial variation of CDW amplitude, we performed an inverse transform of CDW FT peaks. Inverse Fourier transform (IFT) image clearly shows diminishing CDW amplitudes in the presence of Ti defects in Figs. 2(d) and 2(g). In the presence of a large number of defects, CDW-modulated regions can be easily visually identified from IFT images [Fig. 2(d)]. In $1T$-TiSe$_2$ with more Ti intercalation density, domains of CDWs are formed by the presence of defects. 2×2 superstructure of CDWs changes to 1×1 modulation near intercalation sites, which forms the boundaries of the CDW-modulated region [Figs. 2(a) and 2(c)]. Also, the IFT image is used as a guide to locate these boundaries.

Different CDW modulated regions are marked in red in Fig. 2(a). CDW-modulated regions separated by boundaries were not observed in Fig. 2(e) containing fewer intercalation sites. IFT in Fig. 2(g) shows the reduced amplitude of CDWs in the presence of intercalation sites but no formation of separate regions. $1T$-TiSe$_2$ thin flakes are reported to oxidize quickly in atmospheric conditions and disrupt the CDW phase [44]. The oxidation of $1T$-TiSe$_2$ was minimized by cleaving the crystals in our UHV sample preparation chamber (refer to Sec. II, Methods). O and I substitution sites increases the DOS in the unoccupied states away from the Fermi energy [41]. The CDW gap near the Fermi level remains unaffected by O or I substitution.

Metal intercalation of $1T$-TiSe$_2$ at certain doping concentrations shows the phase shift of CDW modulation across the domain walls [26,45]. Cu intercalation in $1T$-TiSe$_2$ results in an ICDW phase with localized CCDWs separated by domain walls at critical doping concentration [46]. Ti, like Cu, is electropositive and suppresses the CDW phase. Cu intercalation into a van der Waals gap of $1T$-TiSe$_2$ was stabilized by transfer of charge from Cu to Se atoms in the adjacent layers [47]. Similarly, the Ti intercalant gets stabilized by charge transfer. A significant overlap between the atomic orbitals
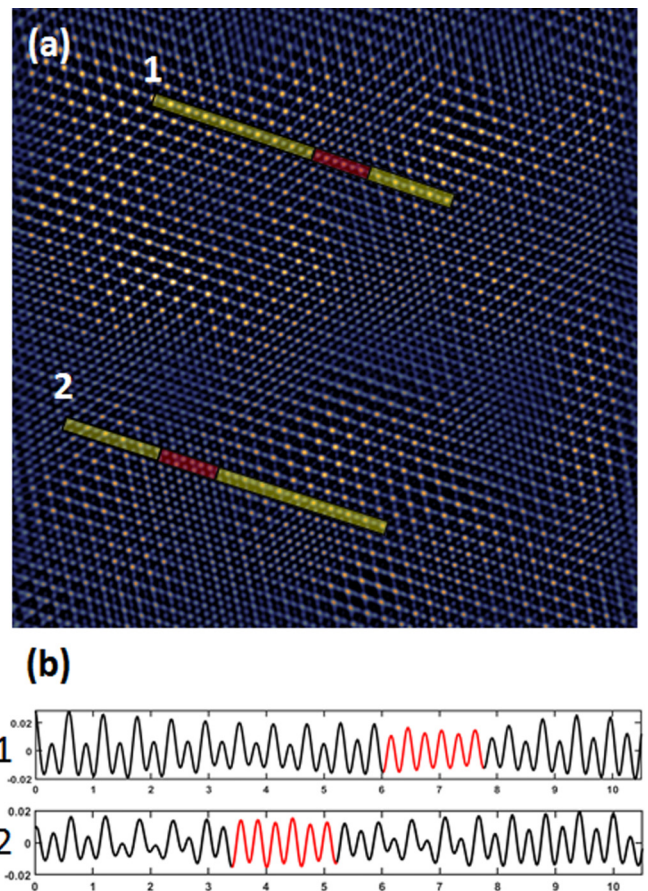

FIG. 3. (a) Inverse Fourier transform image of Bragg peaks and CDW peaks of STM image shown in Fig. 2(a) of sample A. Line sections 1 and 2 passing through domain boundary (marked by red region) plotted in (b). Red part of line section indicates no CDW modulation. No phase shift observed across the domain wall.

of intercalated Ti and Se atoms in the layer results in the intercalant sites' peculiar appearance in the STM images. To better understand the phase shift of CDWs across domain boundaries, IFT of both lattice Bragg peaks and CDW peaks of Fig. 2(a) were obtained, as shown in Fig. 3(a). A line section of electron density indicates the suppression of CDW modulation at the boundary [Fig. 3(b)].

Interestingly, we observed no phase shift in the CDW modulation across the boundaries. We can infer that the increased concentration of Ti intercalation leads to the disruption of CDW and reduces long-range order to small regions [48].

The electropositive nature of Ti intercalation defects and the formation of CDW-modulated regions and nonmodulated boundaries in excess Ti intercalation may provide some insight into the mechanism of formation of CDWs. Considering the results mentioned above, we offer a hypothesis for suppression of CDWs by Ti intercalation. Semimetals or small gap semiconductors at lower temperatures can undergo a CDW phase transition by excitonic condensation mechanism. An exciton is a bound state of electrons and holes, mediated by Coulomb interaction, a composite boson. For $1T$-TiSe$_2$, a small carrier density and a weakly screened Coulomb interaction can result in exciton formation. Excitons are formed from electrons in the pocket at the L point in the Brillouin zone (BZ) and holes from the pocket at Γ point in the energy band structure of $1T$-TiSe$_2$. Being a composite boson, it undergoes condensation at $T_{CDW} \sim 200$ K as the number of excitons increases. Excitonic condensation leads to a periodic modulation of charge density, a CDW state. The extent to which CDWs are modulated in $1T$-TiSe$_2$ is intercalation dependent. If we assume excitonic condensation as the mechanism of CDW state in $1T$-TiSe$_2$ then the suppression of CDWs and

formation of domain boundaries can be explained by the electropositive nature of Ti intercalation.

The first-principles energy band calculations show that the electron pocket at the L point in BZ is derived mainly from Ti $3d$ states. Hole pockets at Γ are derived from Se $2p$ states hybridized with Ti $3d$ states [49]. At Fermi energy, more than half the DOS results from Ti states and the rest comes from Se [47]. As Ti intercalation's character is electropositive, the addition of Ti results in the acquisition of electrons. Because of Ti's larger DOS, electrons added to the system go to Ti derived states around the Fermi level. Ti intercalation now causes the enhancement of electronic states at Fermi energy, resulting in the strong screening of Coulomb interaction between electrons and holes. This screening results in the reduction of excitonic pair and suppression of CDWs.

To further characterize the CDW order, we have calculated the translational correlation. Calculating the correlation length of CDWs using topographic images can shed light on the interplay between CDWs and intercalant density. Nonmodulated boundaries of CDW modulated regions can be easily identified visually from STM topography images of areas with large defect concentration as in Fig. 3(a). Correlation length can be used to gauge the disruption of CDW order because of intercalation. Correlation length measurements can pick up the change in CDW order where it is not easily discernible from STM images visually. The presence of intercalants disrupts the CDW order and hence results in a reduced translational correlation length.

CDW peaks in the FT of topography images were selected and IFT was performed. The IFT image displays CDW amplitudes as a function of position [as in Figs. 2(d) and 2(g)]. Autocorrelation of this image provides information about the
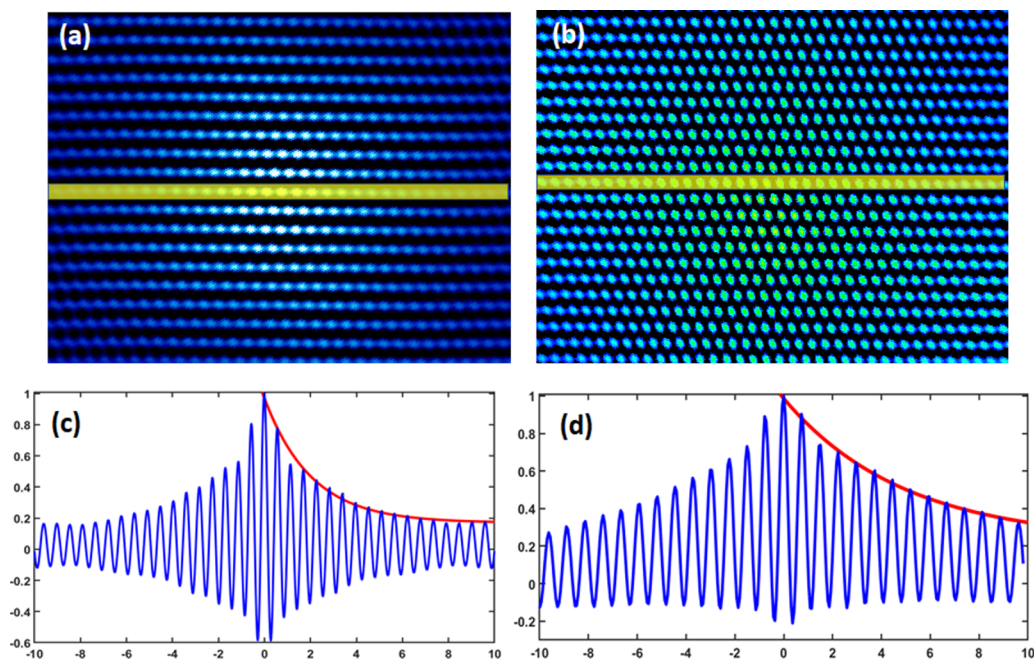

FIG. 4. (a) Autocorrelation of 30 nm x 30 nm area of sample A. (b) Autocorrelation of 30 nm x 30 nm area of sample B. (c), (d) Line section of autocorrelation of sample A shown in (a) and autocorrelation of sample B shown in (b) along the CDW direction, respectively, red curve indicates the rate of decay of CDW amplitude.
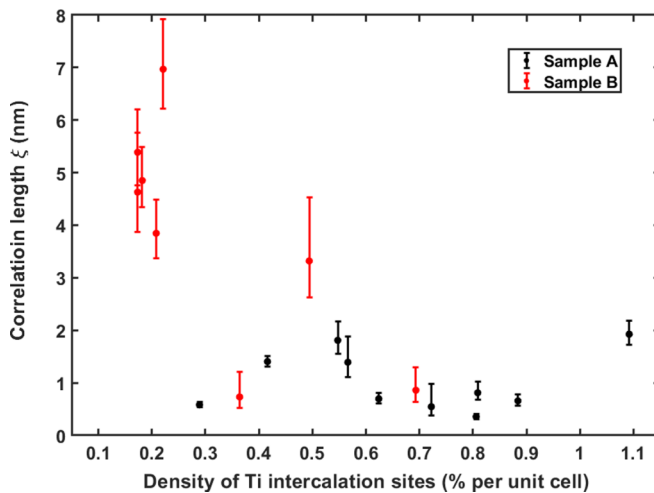
FIG. 5. Correlation length obtained by fitting the CDW amplitudes for topography images of different Ti intercalation concentrations. Sample A contains more intercalation sites than sample B. (The average density of intercalation sites for sample A is 0.6% and for sample B is 0.2%.) Correlation length of CDWs in sample B seems to be higher than that of CDWs in sample A.

translational correlation length. The correlation length was obtained by calculating the change in amplitude of CDW from line sections in the auto correlation of IFT images, using the following equation [50]:

$$A(x) = A_0 e^{-x/\xi} \cos(k_{cdw}x) + B_0, \qquad (1)$$

where $A(x)$ is CDW amplitude, ξ is correlation length, k_{cdw} wave vector of CDW in x direction, B_0 is average random noise in autocorrelation obtained from IFT, and $A_0 = 1 - B_0$. The finite correlation length is a consequence of the inhomogeneity and finite scanning area [50]. The autocorrelation of a STM topography image of an area with more defects in Fig. 2(a) is shown in Fig. 4(a) and an area with a fewer number of defects in Fig. 2(e) is shown in Fig. 4(b). A line section along the axis in an autocorrelation image that is the amplitude of CDW as a function of x was plotted. The correlation length was calculated by a fitting curve to the decay rate of amplitude in the line section. In Figs. 4(b) and 4(d), the blue curve is a line section along CDW direction, indicating its amplitude, and the red curve fitted using Eq. (1) shows a rate of change of CDW amplitude. The correlation length obtained from fitting indicates that the correlation length is smaller for images with more intercalant sites than images with fewer intercalant sites. This implies the long-range coherence of CDWs has broken into small domains because of intercalation. A sharp decline of CDW amplitudes means a smaller correlation length, which is a sign of the reduced long-range order.

The correlation length of CDWs is a function of the concentration of Ti intercalation. A better picture of the exact dependence of correlation length on Ti intercalation density can be obtained by plotting the correlation length, as shown in Fig. 5. Atomically resolved images were taken and the number of Ti intercalation sites were counted. The correlation length of CDWs was calculated from the autocorrelation of IFT images, as mentioned above. Ti intercalation concentration in sample B is less than sample A and shows a large correlation length. The overall trend indicates that the correlation length of CDWs decreases as the Ti intercalation increases. The dependence of correlation length on electron doping nature of Ti intercalant strongly supports our hypothesis discussed in the earlier part of the excitonic origin of CDWs. However, there are certain features in the graph that require close examination. The correlation length tends to increase gradually at defect concentration of 0.3%, reaching maxima at 0.5% then decrease again. This feature could be connected to the inequivalent Ti defect sites for each defect that are a consequence of CDW modulation [48]. We believe our experimental result will motivate further detailed density-functional theory-based calculations to explain this pattern in our correlation length.

IV. CONCLUSIONS

We have explored defects at the atomic scale in two crystals of $1T$-TiSe$_2$ grown using different methods. Ti atoms get intercalated in the van der Waals gap. We find that the density of Ti intercalation affects the long-range order of CDWs. An increased concentration of Ti intercalation forces CDWs to form domains. There is no phase shift across the domain walls. The correlation length of CDWs is inversely proportional to the density of intercalated Ti atoms. Intercalation of Ti in $1T$-TiSe$_2$ suppresses CDWs and forms domain boundaries that can be explained by the electron doping nature of Ti. Intercalated Ti atoms reduce the number of holes in the system. In the excitonic condensation model of CDW formation, the reduction of hole concentration depletes excitonic bound states. CDW suppression is a direct consequence of excitonic bound-state depletion. Thus we demonstrate that our study of the dependence of correlation length on Ti intercalation supports the excitonic condensation model of formation of CDWs in $1T$-TiSe$_2$.

[1] A. A. Tedstone, D. J. Lewis, and P. O'Brien, Chem. Mater. **28**, 1965 (2016).

[2] T. Mueller and E. Malic, npj 2D Mater. Appl. **2**, 1 (2018).

[3] I. Pallecchi, N. Manca, B. Patil, L. Pellegrino, and D. Marré, Nano Futures **4**, 032008 (2020).

[4] H. Huang, X. Fan, D. J. Singh, and W. T. Zheng, Nanoscale **12**, 1247 (2020).

[5] A. V. Kolobov and J. Tominaga, *Two-Dimensional Transition-Metal Dichalcogenides*, 1st ed., Springer Series in Materials Science, Vol. 239 (Springer, New York, 2016).

[6] H. Isomaki and J. Von Boehm, J. Phys. C. **14**, L75 (1981).

[7] F. J. Di Salvo, D. Moncton, and J. Waszczak, Phys. Rev. B **14**, 4321 (1976).

[8] G. Grüner, Rev. Mod. Phys. **60**, 1129 (1988).

[9] K. Rossnagel, J. Phys.: Condens. Matter **23**, 213001 (2011).

[10] L. Li, E. O'Farrell, K. Loh, G. Eda, B. Özyilmaz, and A. C. Neto, Nature **529**, 185 (2016).

[11] E. Morosan, H. W. Zandbergen, B. Dennis, J. Bos, Y. Onose, T. Klimczuk, A. Ramirez, N. Ong, and R. J. Cava, Nat. Phys. **2**, 544 (2006).

[12] Y. I. Joe, X. Chen, P. Ghaemi, K. Finkelstein, G. de La Peña, Y. Gan, J. Lee, S. Yuan, J. Geck, G. MacDougall *et al.*, Nat. Phys. **10**, 421 (2014).

[13] A. Kogar, G. A. de la Pena, S. Lee, Y. Fang, S. X.-L. Sun, D. B. Lioi, G. Karapetrov, K. D. Finkelstein, J. P. C. Ruff, P. Abbamonte, and S. Rosenkranz, Phys. Rev. Lett. **118**, 027002 (2017).

[14] D. Jérome, T. Rice, and W. Kohn, Phys. Rev. **158**, 462 (1967).

[15] H. Hughes, J. Phys. C: Solid State Phys. **10**, L319 (1977).

[16] J. Kuneš, J. Phys.: Condens. Matter **27**, 333201 (2015).

[17] K. Seki, Y. Wakisaka, T. Kaneko, T. Toriyama, T. Konishi, T. Sudayama, N. L. Saini, M. Arita, H. Namatame, M. Taniguchi, N. Katayama, M. Nohara, H. Takagi, T. Mizokawa, and Y. Ohta, Phys. Rev. B **90**, 155116 (2014).

[18] A. Brinkman and H. Hilgenkamp, Phys. C **422**, 71 (2005).

[19] Z. Wang, D. A. Rhodes, K. Watanabe, T. Taniguchi, J. C. Hone, J. Shan, and K. F. Mak, Nature **574**, 76 (2019).

[20] A. S. Shkvarin, A. I. Merentsov, N. Tsud, and A. N. Titov, Inorg. Chem. **60**, 185 (2021).

[21] L. Krasavin, A. Titov, and V. Antropov, Phys. Solid State **40**, 1962 (1998).

[22] M. D. Watson, O. J. Clark, F. Mazzola, I. Marković, V. Sunko, T. K. Kim, K. Rossnagel, and P. D. C. King, Phys. Rev. Lett. **122**, 076404 (2019).

[23] P. Chen, Y.-H. Chan, X.-Y. Fang, Y. Zhang, M.-Y. Chou, S.-K. Mo, Z. Hussain, A.-V. Fedorov, and T.-C. Chiang, Nat. Commun. **6**, 8943 (2015).

[24] K. Rossnagel, L. Kipp, and M. Skibowski, Phys. Rev. B **65**, 235101 (2002).

[25] H. Cercellier, C. Monney, F. Clerc, C. Battaglia, L. Despont, M. G. Garnier, H. Beck, P. Aebi, L. Patthey, H. Berger, and L. Forro, Phys. Rev. Lett. **99**, 146403 (2007).

[26] B. Hildebrand, T. Jaouen, C. Didiot, E. Razzoli, G. Monney, M.-L. Mottas, A. Ubaldini, H. Berger, C. Barreteau, H. Beck *et al.*, Phys. Rev. B **93**, 125140 (2016).

[27] C. Monney, H. Cercellier, F. Clerc, C. Battaglia, E. F. Schwier, C. Didiot, M. G. Garnier, H. Beck, P. Aebi, H. Berger, L. Forro, and L. Patthey, Phys. Rev. B **79**, 045116 (2009).

[28] C. Monney, C. Battaglia, H. Cercellier, P. Aebi, and H. Beck, Phys. Rev. Lett. **106**, 106404 (2011).

[29] M. Cazzaniga, H. Cercellier, M. Holzmann, C. Monney, P. Aebi, G. Onida, and V. Olevano, Phys. Rev. B **85**, 195111 (2012).

[30] A. Kogar, M. S. Rak, S. Vig, A. A. Husain, F. Flicker, Y. I. Joe, L. Venema, G. J. MacDougall, T. C. Chiang, E. Fradkin *et al.*, Science **358**, 1314 (2017).

[31] D. Snoke, Science **298**, 1368 (2002).

[32] W. Kohn and D. Sherrington, Rev. Mod. Phys. **42**, 1 (1970).

[33] J. Ishioka, Y. H. Liu, K. Shimatake, T. Kurosawa, K. Ichimura, Y. Toda, M. Oda, and S. Tanda, Phys. Rev. Lett. **105**, 176401 (2010).

[34] J. Ishioka, T. Fujii, K. Katono, K. Ichimura, T. Kurosawa, M. Oda, and S. Tanda, Phys. Rev. B **84**, 245125 (2011).

[35] M. Iavarone, R. Di Capua, X. Zhang, M. Golalikhani, S. A. Moore, and G. Karapetrov, Phys. Rev. B **85**, 155103 (2012).

[36] A. F. Kusmartseva, B. Sipos, H. Berger, L. Forro, and E. Tutiš, Phys. Rev. Lett. **103**, 236401 (2009).

[37] E. Morosan, K. E. Wagner, L. L. Zhao, Y. Hor, A. J. Williams, J. Tao, Y. Zhu, and R. J. Cava, Phys. Rev. B **81**, 094524 (2010).

[38] J. S. Chen, J. K. Wang, S. V. Carr, S. C. Vogel, O. Gourdon, P. Dai, and E. Morosan, Phys. Rev. B **91**, 045125 (2015).

[39] 2D Semiconductors Inc., USA (2018), https://www.2dsemiconductors.com.

[40] C. G. Slough, B. Giambattista, A. Johnson, W. W. McNairy, C. Wang, and R. V. Coleman, Phys. Rev. B **37**, 6571 (1988).

[41] B. Hildebrand, C. Didiot, A. M. Novello, G. Monney, A. Scarfato, A. Ubaldini, H. Berger, D. R. Bowler, C. Renner, and P. Aebi, Phys. Rev. Lett. **112**, 197001 (2014).

[42] S. Fan, X. Zou, H. Du, L. Gan, C. Xu, W. Lv, Y.-B. He, Q.-H. Yang, F. Kang, and J. Li, J. Phys. Chem. C **121**, 13599 (2017).

[43] M. M. May, C. Brabetz, C. Janowitz, and R. Manzke, J. Electron Spectrosc. Relat. Phenom. **184**, 180 (2011).

[44] L. Sun, C. Chen, Q. Zhang, C. Sohrt, T. Zhao, G. Xu, J. Wang, D. Wang, K. Rossnagel, L. Gu *et al.*, Angew. Chem., Int. Ed. **56**, 8981 (2017).

[45] T. Jaouen, B. Hildebrand, M.-L. Mottas, M. Di Giovannantonio, P. Ruffieux, M. Rumo, C. W. Nicholson, E. Razzoli, C. Barreteau, A. Ubaldini *et al.*, Phys. Rev. B **100**, 075152 (2019).

[46] S. Yan, D. Iaia, E. Morosan, E. Fradkin, P. Abbamonte, and V. Madhavan, Phys. Rev. Lett. **118**, 106405 (2017).

[47] R. A. Jishi and H. M. Alyahyaei, Phys. Rev. B **78**, 144516 (2008).

[48] A. M. Novello, B. Hildebrand, A. Scarfato, C. Didiot, G. Monney, A. Ubaldini, H. Berger, D. R. Bowler, P. Aebi, and C. Renner, Phys. Rev. B **92**, 081101(R) (2015).

[49] A. Zunger and A. J. Freeman, Phys. Rev. B **17**, 1839 (1978).

[50] C. J. Arguello, S. P. Chockalingam, E. P. Rosenthal, L. Zhao, C. Gutiérrez, J. H. Kang, W. C. Chung, R. M. Fernandes, S. Jia, A. J. Millis, R.J. Cava, and A. N. Pasupathy, Phys. Rev. B **89**, 235115 (2014).